




## Discrete unified gas kinetic scheme for continuum compressible flows

Zhaoli Guo (郭照立) <sup>1,\*</sup>, Lian-Ping Wang (王连平) <sup>2,†</sup> and Yiming Qi (岐亦铭) <sup>3</sup>

<sup>1</sup>*Institute of Multidisciplinary Research for Mathematics and Applied Science, Huazhong University of Science and Technology, Wuhan 430074, China*

<sup>2</sup>*Department of Mechanics and Aerospace Engineering, Southern University of Science and Technology, Shenzhen 518055, China*

<sup>3</sup>*State Key Laboratory for Turbulence and Complex Systems, College of Engineering, Peking University, Beijing 100871, China*



(Received 19 October 2022; revised 18 January 2023; accepted 24 January 2023; published 10 February 2023)

In this paper, a discrete unified gas kinetic scheme (DUGKS) is proposed for continuum compressible gas flows based on the total energy kinetic model [Guo *et al.*, *Phys. Rev. E* **75**, 036704 (2007)]. The proposed DUGKS can be viewed as a special finite-volume lattice Boltzmann method for the compressible Navier-Stokes equations in the double distribution function formulation, in which the mass and momentum transport are described by the kinetic equation for a density distribution function ( $g$ ), and the energy transport is described by the other one for an energy distribution function ( $h$ ). To recover the full compressible Navier-Stokes equations exactly, the corresponding equilibrium distribution functions  $g^{eq}$  and  $h^{eq}$  are expanded as Hermite polynomials up to third and second orders, respectively. The velocity spaces for the kinetic equations are discretized according to the seventh and fifth Gauss-Hermite quadratures. Consequently, the computational efficiency of the present DUGKS can be much improved in comparison with previous versions using more discrete velocities required by the ninth Gauss-Hermite quadrature.

DOI: [10.1103/PhysRevE.107.025304](https://doi.org/10.1103/PhysRevE.107.025304)

### I. INTRODUCTION

Numerical methods for simulating continuum compressible flows are mainly designed based on the Navier-Stokes equations. In recent decades, there have been increasing interests to develop kinetic schemes for such flows based on the Boltzmann equation or simplified models. Generally, the kinetic methods for compressible Navier-Stokes equations can be classified into two categories according to the treatment of molecular velocity, namely, the continuous velocity method approach and discrete velocity method (DVM) approach. The former solves the compressible Navier-Stokes equations, where the particle distribution function with continuous molecular velocity  $\xi$  is used to construct the numerical flux at cell interface. A typical example of this type is the gas-kinetic scheme (GKS) [1]. The DVM solves the kinetic equation directly, with full discretizations in time, physical space, and velocity space. Particularly, the continuous velocity space is discretized into a discrete velocity set (DVS)  $V_k \equiv \{\xi_i\}$ ,  $i = 0, 1, \dots, b - 1$ . Typical methods of such type include the discrete ordinate method (DOM) [2], implicit-explicit (IMEX) method [3], unified gas kinetic scheme (UGKS) [4] and discrete UGKS (DUGKS) [5]. The aforementioned DV methods are mainly designed for rarefied gas flows covering a wide range of flow regimes, particularly for noncontinuum flows. For continuous compressible flows, the efficiency of these methods is usually not acceptable due to the large number of discrete velocities.

On the other hand, the lattice Boltzmann equation (LBE) [6], which can be viewed as a special DVM with the use of a certain regular lattice and associated space-time discretization, can take an optimized DVS such that the computational efficiency can be enhanced. Actually, some comparisons between LBE and Navier-Stokes solvers for continuum flows (e.g., [7,8]), and kinetic methods for rarefied flows, have been reported (e.g., [9,10]). These comparisons demonstrate that the LBE, although is of second-order accuracy, generally has better dissipative and dispersion properties than second-order Navier-Stokes solvers [7], and can even be more efficient [8]. Most LBE models and applications in the literature concentrate on athermal (nearly) incompressible flows, where only mass and momentum are conserved (defined by the zeroth- and first-order moments of the discrete distribution function, respectively). Enormous efforts have been devoted to developing LBE models for fully compressible flows with low or high Mach numbers. Compared with incompressible LBE, the energy equation must be solved consistently in compressible LBE. To this end, different strategies have been proposed. The early compressible LBE models (e.g., [11–13]) extended the athermal counterparts by enforcing the energy conservation (defined from the second-order moment of the distribution function) with enlarged DVS's and higher-order equilibrium distribution functions. However, these multispeed LBE models usually suffer from severe numerical instability, which can be attributed to the violation of the Courant-Friedrichs-Lewy (CFL) number due to the high-speed discrete velocities [14,15], or to the coupling between the shear mode and energy mode that makes the scheme sensitive to fluctuations of wide-ranged scales [16]. This difficulty can be alleviated by treating the energy equation independently from the mass and

\*zlguo@mail.hust.edu.cn

†wanglp@sustech.edu.cn

momentum equations, which can be realized by different strategies such as the double distribution function (DDF) approach and the hybrid approach. In a DDF model, the evolution of mass and momentum is described by an LBE for a density distribution function and the energy transfer is solved by another LBE for an energy distribution function. Originally, the DDF approach was adopted to design LBE models for nearly incompressible thermal flows where the density and temperature variations are small (e.g., [17–20]), and this approach was applied to compressible flows with shock discontinuities (e.g., [21–23]) later. In the hybrid approach, the mass and momentum conservations are still solved by LBE, while the energy conservation is solved by classical numerical schemes such as the finite-difference or finite-volume methods [24–26]. A comprehensive linear stability analysis of hybrid LBE models was provided recently [27], which demonstrates that the numerical stability of such models depends on a number of factors such as energy variables, formulations, collision terms, and numerical discretizations.

The choice of DVS  $V_k$  is one of the most critical points for compressible LBE models. Three types of DVS are used in the current studies, namely, on-lattice, off-lattice, and adaptive ones. Both on-lattice and off-lattice DVS's are fixed in the computation, while the adaptive DVS depends on local fluid velocity and/or temperature and thus changes with time and position. The discrete velocities in the on-lattice DVS are coupled tightly with the underlying space lattice, such that the LBM can be implemented in a Lagrangian manner following the collision-streaming procedure. Consequently, the algorithm is simple and numerical dissipation is low. On-lattice DVS has been adopted in the multispeed, DDF, and hybrid LBE models [11,21,24]. Usually, in order to describe the full compressible Navier-Stokes equations by the multispeed LBE, the zeroth through fourth-order continuous velocity moments of the equilibrium distribution function should be realized exactly by the corresponding discrete moments [28], such that a large on-lattice DVS is required and the computational cost is rather high. Furthermore, the DVS also influences the numerical stability and Mach number limit, and a detailed analysis for the choice of admissible higher-order lattices was presented [29]. On the other hand, the DDF and hybrid LBE models can use a smaller  $V_k$  due to the decoupling of energy equation from mass and momentum equations. Particularly, the DVS used in athermal LBE can be adopted [22,25,26,30,31]. However, in order to recover the intrinsic coupling between these conservative variables, some nontrivial correction terms are required. An alternative strategy for reducing the number of discrete velocities is to abandon the coupling between the DVS and lattice, namely, using off-lattice discrete velocities. As such, the standard collision-streaming procedure of LBE cannot be implemented in LBE with an off-lattice DVS. Generally, Eulerian or semi-Lagrangian discretizations of the discrete velocity kinetic equation (DVKE) can be employed [32–38]. Unlike the fixed on-lattice and off-lattice DVSS, a dynamic velocity set changes with the local fluid velocity and/or temperature, such that it can cover a large velocity range, which is necessary for simulating high Mach flows. LBE with a dynamic velocity set can be traced back to the work of Sun [39], and recently was reinterpreted by Dorschner

*et al.* [40]. Generally, interpolations are needed, which not only increase the complexity of the algorithms but also destroy conservation. A more serious problem of such LBE methods lies in the noncommutation between the particle velocity  $\xi_i$  and the temporal and spatial derivatives,  $\partial_t(\xi_i\phi) \neq \xi_i\partial_t\phi$  and  $\nabla \cdot (\xi_i\phi) \neq \xi_i \cdot \nabla\phi$  for a space- and time-changing variable  $\phi(x, t)$ , which will lead to incorrect hydrodynamic equations from the DVKE [6]. Based on the above analysis, we conclude that the fixed off-lattice DVS is preferred to design reliable and efficient LBE methods for compressible flows.

Once a fixed off-lattice DVS is chosen, the DVKE can be solved using different numerical methods, such as finite-difference, finite-volume, or semi-Lagrangian methods [32–38]. Generally, a finite-difference kinetic scheme may suffer from poor numerical stability or large numerical dissipation even if the IMEX strategy is adopted [32], while semi-Lagrangian schemes require certain space interpolations for the distribution function at starting point, which may influence the conservation property of the method and brings difficulties in treating boundary conditions. On the contrary, finite-volume discretizations of the DVKE can ensure the exact conservation, and boundary conditions can be realized easily. The first finite-volume LBE (FV-LBE) method was due to Nannelli and Succi [41] for nearly incompressible flows, and later some alternative formulations were developed [42–44]. FV-LBE schemes for compressible flows were also developed, e.g., Ref. [45]. A general problem of the aforementioned FV-LBE methods is that the time step is limited by the collision time due to numerical dissipation and stability requirements [43,46]. This problem can be attributed to the negligence of collision effect in the flux reconstruction and the explicit treatment of the collision term [47,48]. Recently, a finite-volume kinetic scheme with the consideration of collision effect in flux reconstruction was proposed [46], which removes the restriction of the relaxation time on the time step. However, this FV-LBE is designed for incompressible flows. A more general finite-volume kinetic scheme in which the collision effect is considered in flux reconstruction is the DUGKS method [5], which was designed originally for multi-scale flows covering a wide range of flow regimes, and can be viewed as special FV-LBE in the continuum limit. Actually, the FV-LBE in [46] can be interpreted as a simplified version of the DUGKS for continuum flows, but with degenerated numerical stability [46]. It was shown the DUGKS exhibits lower numerical dissipation and better numerical stability than an advanced FV-LBE [49], and DUGKS has also been employed to study thermal and compressible flows [50–52]. As a special discrete velocity method, DUGKS shares the common difficulty of expensive computational costs in simulating compressible flows, due to the requirement of a large DVS. Therefore, more efficient DUGKS with less discrete velocities for compressible flows is still desired.

A systemic approach for determining the DVS was provided based on Hermite expansion of the distribution function and Gauss-Hermite quadrature [28]. It is shown that a Gauss-Hermite quadrature of at least eighth degree of precision is required in order to recover the fully compressible Navier-Stokes equations from the Bhatnagar-Gross-Krook (BGK) Boltzmann equation via the Chapman-Enskog

expansion. With this approach, some two-dimensional (2D) and three-dimensional (3D) on-lattice and off-lattice discrete velocity sets have been designed [53], denoted, respectively, by  $DnQb-Ax$  and  $DnVb-Ax$ , representing  $n$ -dimensional  $b$ -velocity of degree- $x$  quadrature precision. Specifically, four minimum D2Q37-A9 sets and one minimum D3Q103-A9 were found [53]. Alternatively, some smaller off-lattice DVS's with the same degree of precision have been found, such as the D3V77-A9 [52] and D3V45-A9 [54] sets. To our best knowledge, the D3V45-A9 set is the available minimum DVS for 3D compressible flows in the literature.

It is noted the employed kinetic model also influences the requirement for DVS. For example, if the Shakhov or ellipsoidal-statistical model with an adjustable Prandtl number is employed to develop discrete-velocity methods, the requirement of Hermite expansion of the equilibrium distribution function and the degree of precision of the Gauss-Hermite quadrature will rise [51,52]. Furthermore, if the DDF approach is adopted, the choice of energy distribution function will also influence the requirement. Generally, three types of energy distribution functions can be used, i.e., internal energy one [17,18], total energy one [20,55], and partial internal energy one [5,52,56]. The D3V77-A9 [52] and D3V45-A9 [54] sets are both determined based on the partial energy distribution function, where a fourth-order Hermite expansion and a quadrature of at least eighth degree are required.

In this work, we aim to develop a more efficient DUGKS for fully compressible flows based on the total energy model [20]. Following the procedure in [28], it is shown that in order to recover the compressible Navier-Stokes equations, we need only third- and second-order Hermite expansions of the equilibrium density and energy distribution functions, together with degree-6 and degree-4 Gauss-Hermite quadratures, respectively. Consequently, the computational costs of the proposed DUGKS can be reduced significantly.

The rest of this article is organized as follows. In Sec. II the Hermite representation of the total energy kinetic model [20] is derived, and the required discrete velocity sets are described. The DUGKS algorithm is presented in Sec. III, and a summary is given in the last section.

## II. HERMITE REPRESENTATION OF THE TOTAL-ENERGY KINETIC MODEL

### A. Total-energy kinetic model

The total-energy kinetic model starts from the BGK Boltzmann equation [57],

$$\partial_t f + \boldsymbol{\xi} \cdot \nabla f = -\frac{1}{\tau}(f - f^{(eq)}), \quad (1)$$

where  $f(\mathbf{x}, \boldsymbol{\xi}, \boldsymbol{\eta}, \boldsymbol{\zeta}, t)$  is the distribution function for molecules moving in  $D$ -dimensional physical space with velocity  $\boldsymbol{\xi} = (\xi_1, \dots, \xi_D)$  at position  $\mathbf{x} = (x_1, \dots, x_D)$  and time  $t$ ,  $\boldsymbol{\eta} = (\eta_{D+1}, \dots, \eta_3)$  is a vector consisting of the remaining  $3 - D$  components of the molecular velocity,  $\boldsymbol{\zeta}$  is a vector of length  $K$ , which can be considered as a parametrization of the internal degrees of freedom of a molecule [57], and  $\tau$  is the relaxation time. Note that particle translation occurs only in the  $\boldsymbol{\xi}$  space, and  $\boldsymbol{\eta}$  can be regarded as a variable representing additional freedoms. The equilibrium distribution function

$f^{(eq)}$  depends on the fluid density  $\rho$ , velocity  $\mathbf{u}$ , and temperature  $T$ ,

$$f^{(eq)} = \frac{\rho}{(2\pi RT)^{(3+K)/2}} \exp\left(-\frac{c^2 + \eta^2 + \zeta^2}{2RT}\right), \quad (2)$$

where  $R$  is the gas constant,  $\mathbf{c} = \boldsymbol{\xi} - \mathbf{u}$  is the peculiar velocity, and  $c^2 = \mathbf{c} \cdot \mathbf{c}$ . The fluid variables  $\rho$ ,  $\mathbf{u}$ , and  $T$  are defined by the velocity moments of  $f$ ,

$$\rho = \int f d\boldsymbol{\xi} d\boldsymbol{\eta} d\boldsymbol{\zeta}, \quad (3a)$$

$$\rho \mathbf{u} = \int \boldsymbol{\xi} f d\boldsymbol{\xi} d\boldsymbol{\eta} d\boldsymbol{\zeta}, \quad (3b)$$

$$\frac{3+K}{2} \rho RT = \int \frac{1}{2}(c^2 + \eta^2 + \zeta^2) f d\boldsymbol{\xi} d\boldsymbol{\eta} d\boldsymbol{\zeta}. \quad (3c)$$

Note that the temperature  $T$  is related to the total energy  $E$ , which is defined by

$$\rho E = \int \frac{1}{2}(\xi^2 + \eta^2 + \zeta^2) f d\boldsymbol{\xi} d\boldsymbol{\eta} d\boldsymbol{\zeta}, \quad (4)$$

i.e.,  $\rho E = \rho \epsilon + \frac{1}{2} \rho u^2$ , with  $\epsilon = c_v T$  being the internal energy and  $c_v = (3+K)R/2$  the specific heat coefficient at constant volume. The pressure tensor  $\mathbf{P}$  and heat flux  $\mathbf{q}$  are given by

$$\mathbf{P} = \int \mathbf{c} \mathbf{c} f d\boldsymbol{\xi} d\boldsymbol{\eta} d\boldsymbol{\zeta}, \quad \mathbf{q} = \int \frac{c^2 + \eta^2 + \zeta^2}{2} \mathbf{c} f d\boldsymbol{\xi} d\boldsymbol{\eta} d\boldsymbol{\zeta}. \quad (5)$$

Note that the variables  $\boldsymbol{\eta}$  and  $\boldsymbol{\zeta}$  have no direct influences on the hydrodynamics. In order to remove the dependence on these two redundant variables, a DDF kinetic model was proposed [20], which uses a density distribution function  $g(\mathbf{x}, \boldsymbol{\xi}, t)$  and a total energy distribution function  $h(\mathbf{x}, \boldsymbol{\xi}, t)$  defined by

$$g(\mathbf{x}, \boldsymbol{\xi}, t) = \int f(\mathbf{x}, \boldsymbol{\xi}, \boldsymbol{\eta}, \boldsymbol{\zeta}, t) d\boldsymbol{\eta} d\boldsymbol{\zeta},$$

$$h(\mathbf{x}, \boldsymbol{\xi}, t) = \int \frac{\xi^2 + \eta^2 + \zeta^2}{2} f(\mathbf{x}, \boldsymbol{\xi}, \boldsymbol{\eta}, t) d\boldsymbol{\eta} d\boldsymbol{\zeta}. \quad (6)$$

The total kinetic model is constructed based on Eq. (1), by separating the collision contribution to the total energy into internal energy part and mechanical energy part that are characterized by different relaxation times [20],

$$\partial_t g + \boldsymbol{\xi} \cdot \nabla g = -\frac{1}{\tau_g}(g - g^{(eq)}), \quad (7a)$$

$$\partial_t h + \boldsymbol{\xi} \cdot \nabla h = -\frac{1}{\tau_h}(h - h^{(eq)}) + \frac{1}{\tau_{hg}} R^z, \quad (7b)$$

where  $\tau_g$  and  $\tau_h$  are two relaxation times characterizing the momentum and energy relaxations, respectively, and  $\tau_{hg}^{-1} = \tau_h^{-1} - \tau_g^{-1}$ ; the two equilibrium distribution functions are given by

$$g^{(eq)}(\boldsymbol{\xi}; \rho, \mathbf{u}, T) = \frac{\rho}{(2\pi RT)^{D/2}} \exp\left[-\frac{(\boldsymbol{\xi} - \mathbf{u})^2}{2RT}\right], \quad (8)$$

$$h^{(eq)}(\boldsymbol{\xi}; \rho, \mathbf{u}, T) = \frac{\xi^2 + (3-D+K)RT}{2} g^{(eq)}, \quad (9)$$

and the term  $R^z$  in Eq. (7b) is defined as

$$R^z = Z(g - g^{(eq)}), \quad (10)$$

with  $Z = \xi \cdot \mathbf{u} - u^2/2$ . Note that  $Z$  can also be simplified to be  $Z = \xi \cdot \mathbf{u}$  without influencing the final Navier-Stokes equations [58]. But for nonequilibrium flows beyond the Navier-Stokes hydrodynamics, the original formulation should be adopted due to the differences in high-order moments [55].

We remark that the use of reduced distribution functions is a common technique in gas kinetic theory, e.g., Refs. [59–61]. It is also noted that the idea of using different relaxation times to characterize the difference in momentum and energy transport was already used in the kinetic theory of Woods [62], in which the two relaxation times are included in the first-order approximation to the distribution function. On the other hand, in the total-energy kinetic model [20], the two relaxation times appear explicitly in the kinetic equations, and the last (correction) term in (7b) is constructed based on the separation of mechanical energy from total energy, which was not reflected in the kinetic theory developed in [62].

Based on the definitions of  $g$  and  $h$ , the fluid density, velocity, and total energy can now be given by the moments of  $g$  and  $h$ ,

$$\rho = \int g d\xi, \quad \rho \mathbf{u} = \int \xi g d\xi, \quad \rho E = \int h d\xi. \quad (11)$$

The pressure tensor  $\mathbf{P}$  and heat flux  $\mathbf{q}$  are given by

$$\mathbf{P} = \int \mathbf{c} \mathbf{c} g d\xi, \quad \mathbf{q} = \int \mathbf{c} (h - Zg) d\xi = \int \mathbf{c} h d\xi - \mathbf{P} \cdot \mathbf{u}. \quad (12)$$

Through the Chapman-Enskog expansion (see details in [20]), the following compressible Navier-Stokes equations can be obtained from the kinetic model (7) up to the first order of the expansion,

$$\partial_t \rho + \nabla \cdot (\rho \mathbf{u}) = 0, \quad (13a)$$

$$\partial_t (\rho \mathbf{u}) + \nabla \cdot (\rho \mathbf{u} \mathbf{u}) = -\nabla p + \nabla \cdot \boldsymbol{\tau}, \quad (13b)$$

$$\partial_t (\rho E) + \nabla \cdot [(p + \rho E) \mathbf{u}] = \nabla \cdot (\kappa \nabla T) + \nabla \cdot (\boldsymbol{\tau} \cdot \mathbf{u}), \quad (13c)$$

where  $p = \rho RT$  is the pressure,  $\boldsymbol{\tau}$  is the stress tensor given by  $\tau_{ij} = 2\mu[S_{ij} - \frac{1}{D}(\nabla \cdot \mathbf{u})\delta_{ij}] + \mu_b(\nabla \cdot \mathbf{u})\delta_{ij}$ , with the strain rate  $S_{ij} = \frac{1}{2}(\partial_i u_j + \partial_j u_i)$ , dynamic viscosity  $\mu = \tau_g p$ , and bulk viscosity  $\mu_b = 2\mu(3 - D + K)/(3 + K)D$ ;  $\kappa = \tau_h c_p p$  is the thermal conductivity, with  $c_p = (5 + K)R/2$  being the specific heat coefficient at constant pressure. It can be seen that the Prandtl number of the total kinetic model (7) is  $\text{Pr} = \mu c_p / \kappa = \tau_g / \tau_h$ , and the specific heat ratio is  $\gamma = c_p / c_v = (5 + K)/(3 + K)$ , while the ratio of bulk to shear viscosity is

$\mu_b / \mu = 2(3 - D + K)/D(3 + K) = 2/D + 1 - \gamma$ . It is obvious that the Prandtl number can be adjusted by changing the two relaxation times, and the specific heat ratio and bulk to shear viscosity ratio depend on the internal freedom of the molecules.

It is noted that in the derivation of Eqs. (13), the following moments of the equilibrium distribution functions are required,

$$\int g^{(eq)} d\xi = \rho, \quad \int \xi g^{(eq)} d\xi = \rho \mathbf{u}, \quad (14a)$$

$$\int \xi_i \xi_j g^{(eq)} d\xi = p \delta_{ij} + \rho u_i u_j, \quad (14b)$$

$$\int \xi_i \xi_j \xi_k g^{(eq)} d\xi = \rho u_i u_j u_k + p(u_i \delta_{jk} + u_j \delta_{ik} + u_k \delta_{ij}), \quad (14b)$$

$$\int h^{(eq)} d\xi = \rho E, \quad \int \xi h^{(eq)} d\xi = (p + \rho E) \mathbf{u},$$

$$\int \xi_i \xi_j h^{(eq)} d\xi = p(RT + E)\delta_{ij} + (2p + \rho E)u_i u_j. \quad (14c)$$

## B. Hermite representation and discrete velocity model

Based on the total energy kinetic model (7), we now derive a discrete velocity kinetic model which can give the compressible Navier-Stokes equation exactly. We follow the approach in [28]. First,  $g^{(eq)}$  and  $h^{(eq)}$  are represented by their Hermite series,

$$g^{(eq)}(\hat{\xi}) \approx g_M^{(eq)}(\hat{\xi}) = \omega(\hat{\xi}) \sum_{n=0}^M \frac{1}{n!} \mathbf{a}^{(n)} \mathbf{H}^{(n)}(\hat{\xi}), \quad (15)$$

$$h^{(eq)}(\hat{\xi}) \approx h_N^{(eq)}(\hat{\xi}) = \omega(\hat{\xi}) \sum_{n=0}^N \frac{1}{n!} \mathbf{b}^{(n)} \mathbf{H}^{(n)}(\hat{\xi}),$$

where  $\hat{\xi} = \xi / \sqrt{RT_0}$  with  $T_0$  being a reference temperature,  $\omega(\hat{\xi}) = (2\pi)^{-D/2} \exp(-\frac{1}{2}|\hat{\xi}|^2)$ ,  $\mathbf{H}^{(n)}(\hat{\xi})$  ( $n = 0, 1, \dots$ ) are the Hermite polynomials,  $M$  and  $N$  are the corresponding truncation orders, and  $\mathbf{a}^{(n)}$  and  $\mathbf{b}^{(n)}$  are the expansion coefficients defined as

$$\mathbf{a}^{(n)} = \int g^{(eq)}(\hat{\xi}) \mathbf{H}^{(n)}(\hat{\xi}) d\hat{\xi}, \quad \mathbf{b}^{(n)} = \int h^{(eq)}(\hat{\xi}) \mathbf{H}^{(n)}(\hat{\xi}) d\hat{\xi}. \quad (16)$$

The key in Hermite representations is to determine the necessary truncation orders  $M$  and  $N$ . From the velocity moments (14) required to recover the compressible Navier-Stokes equations, we realize that the Hermite expansion of  $g^{(eq)}$  in Eq. (7a) must be kept up to  $M = 3$  at least, while those of  $h^{(eq)}$  and  $g^{(eq)}$  in Eq. (7b) must be kept up to  $N = 2$  at least. The explicit expansions can then be written as

$$g^{(eq)} = g_3^{(eq)}(\hat{\xi}) = \rho \omega(\hat{\xi}) \left\{ 1 + \hat{\xi} \cdot \hat{\mathbf{u}} + \frac{1}{2} [(\hat{\xi} \cdot \hat{\mathbf{u}})^2 - \hat{u}^2 + (\theta - 1)(\hat{\xi}^2 - D)] + \frac{1}{6} (\hat{\xi} \cdot \hat{\mathbf{u}}) [(\hat{\xi} \cdot \hat{\mathbf{u}})^2 - 3\hat{u}^2 + 3(\theta - 1)(\hat{\xi}^2 - D - 2)] \right\}, \quad (17)$$

$$h^{(eq)} = h_2^{(eq)}(\hat{\xi}) = \omega(\hat{\xi}) p [(\hat{\xi} \cdot \hat{\mathbf{u}}) + (\hat{\xi} \cdot \hat{\mathbf{u}})^2 - \hat{u}^2 + \frac{1}{2} \theta (\hat{\xi}^2 - D)] + E g_2^{(eq)}, \quad (18)$$

with

$$g_2^{(eq)}(\hat{\xi}) = \rho \omega(\hat{\xi}) \left\{ 1 + \hat{\xi} \cdot \hat{\mathbf{u}} + \frac{1}{2} [(\hat{\xi} \cdot \hat{\mathbf{u}})^2 - \hat{u}^2 + (\theta - 1)(\hat{\xi}^2 - D)] \right\}. \quad (19)$$

TABLE I. Abscissae  $\hat{\xi}_i$  and weights  $w_i$  for several 3D and 2D discrete velocity sets. “cycle” means cycle permutation. DnVb–Ak means a DVS with  $b$  discrete velocities for  $D$ -dimensional space exhibiting degree- $k$  quadrature precision. Data are compiled from [28].

DVS	$\hat{\xi}_i$	$w_i$	
D2V6-A4	(0, 0)	1/2	
	$2(\cos \theta_k, \sin \theta_k)$	1/10	$\theta_k = 2k\pi/5, k = 1 \sim 5$
D2V7-A5	(0, 0)	1/2	
	$2(\cos \theta_k, \sin \theta_k)$	1/12	$\theta_k = k\pi/3, k = 1 \sim 6$
D2V12-A7	$(\pm r, 0)$ (cycle)	1/36	$r = \sqrt{6}$
	$(\pm s, \pm s)$	$(5 + 2\sqrt{5})/45$	$s = \sqrt{9 - 3\sqrt{5}}/2$
	$(\pm q, \pm q)$	$(5 - 2\sqrt{5})/45$	$q = \sqrt{9 + 3\sqrt{5}}/2$
D3V13-A5	(0, 0, 0)	2/5	$r = \sqrt{(5 + \sqrt{5})/2}$
	$(\pm r, \pm s, 0)$ (cycle)	1/20	$s = \sqrt{(5 - \sqrt{5})/2}$
D3V27-A7	(0, 0, 0)	$(720 \pm 8\sqrt{15})/2205$	
	$(\pm r, 0, 0)$ (cycle)	$(270 \mp 46\sqrt{15})/15435$	$r = \sqrt{(15 \pm \sqrt{15})/2}$
	$(\pm s, \pm s, 0)$ (cycle)	$(162 \pm 41\sqrt{15})/6174$	$s = \sqrt{6 \mp \sqrt{15}}$
	$(\pm q, \pm q, \pm q)$	$(783 \mp 202\sqrt{15})/24696$	$q = \sqrt{9 \pm 2\sqrt{15}}$

Here  $\hat{\mathbf{u}} = \mathbf{u}/\sqrt{RT_0}$  and  $\theta = T/T_0$ . Note that  $g_2^{(eq)}$  is also used in the second term ( $Z$  term) on the right-hand side of Eq. (7b).

Now we consider the velocity discretization for the kinetic model (7) with the expanded equilibrium distribution functions  $g_3^{(eq)}$  and  $h_2^{(eq)}$ . The natural choice for determining the DVS's is to use the abscissae of certain Gauss-Hermite quadratures with weight function  $\omega(\hat{\xi})$  such that the velocity moments (14) hold exactly for  $g_3^{(eq)}$  and  $h_2^{(eq)}$ , namely,

$$\int \hat{\xi}^m g_3^{(eq)}(\hat{\xi}) d\hat{\xi} = \int \hat{\xi}^m \omega(\hat{\xi}) [\omega^{-1}(\hat{\xi}) g_3^{(eq)}(\hat{\xi})] d\hat{\xi} = \sum_k w_k \hat{\xi}_k^m [\omega^{-1}(\hat{\xi}_k) g_3^{(eq)}(\hat{\xi}_k)], \quad m = 0, 1, 2, 3, \quad (20)$$

$$\int \hat{\xi}^n h_2^{(eq)}(\hat{\xi}') d\hat{\xi}' = \int \hat{\xi}^n \omega(\hat{\xi}') [\omega^{-1}(\hat{\xi}') h_2^{(eq)}(\hat{\xi}')] d\hat{\xi}' = \sum_l w_l' \hat{\xi}_l'^n [\omega^{-1}(\hat{\xi}_l') h_2^{(eq)}(\hat{\xi}_l')], \quad n = 0, 1, 2, \quad (21)$$

where  $\hat{\xi}_k$  ( $w_k$ ) and  $\hat{\xi}_l'$  ( $w_l'$ ) are the corresponding abscissae (weights) of the quadratures, respectively. We will denote such a DVS by  $\mathcal{V}_K = \{(w_i, \xi_i), i = 1, 2, \dots, K\}$ . Note that  $\omega^{-1}(\hat{\xi}) g_3^{(eq)}(\hat{\xi})$  and  $\omega^{-1}(\hat{\xi}') h_2^{(eq)}(\hat{\xi}')$  are degree-3 and degree-2 polynomials of  $\hat{\xi}$  and  $\hat{\xi}'$ , respectively. Therefore, a quadrature of degree 6 at least is required for evaluating the moments (20), and a quadrature of degree 4 at least is needed for (21). For instance, we can use the D3V27-A7 and D3V13-A5 for  $g_3^{(eq)}$  and  $h_2^{(eq)}$  (and  $g_2^{(eq)}$ ) in the 3D case, respectively. Several DVSs satisfying the requirements are listed in Table I. Note that two choices are available for D3V27-A7, and we denote that with the upper signs as Group I, and the other one as Group II.

With the chosen discrete velocity sets, the distribution functions  $g(\xi)$  and  $h(\xi)$  can be represented by their discrete velocity counterparts. Defining  $g_k = w_k \omega^{-1}(\hat{\xi}_k) g(\hat{\xi}_k)$ , then its kinetic equation can be obtained from Eq. (7a),

$$\partial_t g_k + \hat{\xi}_k \cdot \nabla g_k = -\frac{1}{\tau_g} [g_k - g_k^{(eq)}], \quad (22)$$

where

$$g_k^{(eq)} = w_k \rho \left\{ 1 + \hat{\xi}_k \cdot \hat{\mathbf{u}} + \frac{1}{2} [(\hat{\xi}_k \cdot \hat{\mathbf{u}})^2 - \hat{u}^2 + (\theta - 1)(\hat{\xi}_k^2 - D)] + \frac{1}{6} (\hat{\xi}_k \cdot \hat{\mathbf{u}}) [(\hat{\xi}_k \cdot \hat{\mathbf{u}})^2 - 3\hat{u}^2 + 3(\theta - 1)(\hat{\xi}_k^2 - D - 2)] \right\}. \quad (23)$$

Accordingly, the hydrodynamic variables can be determined as

$$\rho = \sum_k g_k, \quad \rho \mathbf{u} = \sum_k \hat{\xi}_k g_k, \quad \mathbf{P} = \sum_k \mathbf{c}_k \mathbf{c}_k g_k, \quad (24)$$

where  $\mathbf{c}_k = \hat{\xi}_k - \mathbf{u}$ .

Unlike the kinetic equation (7a) which contains only the distribution function  $g$ , the kinetic equation (7b) depends on not only  $h$  but also  $g$  appearing in  $R^z$ . Consequently, the treatment of  $R^z$  in Eq. (7b) needs special care in deriving the discrete kinetic equation. Specifically, if the same DVS is

employed for both (7a) and (7b) (say D2V12-A7 or D3V27-A7), it is straightforward to obtain the DVKE for  $h$ ,

$$\partial_t h_k + \hat{\xi}_k \cdot \nabla h_k = -\frac{1}{\tau_h} (h_k - h_k^{(eq)}) + \frac{1}{\tau_{hg}} R_k^z, \quad (25)$$

where  $h_k = w_k h(\hat{\xi}_k) / \omega(\hat{\xi}_k)$ ,  $Z_k = \hat{\xi}_k \cdot \mathbf{u} - u^2/2$ , and

$$R_k^z = Z_k (g_k - g_{2,k}^{(eq)}), \quad (26)$$

with  $Z_k = \hat{\xi}_k \cdot \mathbf{u} - u^2/2$ , and

$$h_k^{(eq)} = w_k p [\hat{\xi}_k \cdot \hat{\mathbf{u}} + (\hat{\xi}_k \cdot \hat{\mathbf{u}})^2 - \hat{u}^2 + \frac{1}{2}\theta(\hat{\xi}_k^2 - D)] + E g_{2,k}^{(eq)}, \quad (27)$$

with

$$g_{2,k}^{(eq)} = w_k \rho \left\{ 1 + \hat{\xi}_k \cdot \hat{\mathbf{u}} + \frac{1}{2} [(\hat{\xi}_k \cdot \hat{\mathbf{u}})^2 - \hat{u}^2 + (\theta - 1)(\hat{\xi}_k^2 - D)] \right\}. \quad (28)$$

Then the energy and heat flux can be calculated by

$$\rho E = \sum_k h_k, \quad \mathbf{q} = \sum_k \mathbf{c}_k (h_k - Z_k g_k) = \sum_k \mathbf{c}_k h_k - \mathbf{P} \cdot \mathbf{u}, \quad (29)$$

with  $\mathbf{c}_k = \hat{\xi}_k - \mathbf{u}$  and  $\mathbf{P} = \sum_k \mathbf{c}_k \mathbf{c}_k g_k$ .

On the other hand, if the DVS for  $h$ ,  $\mathcal{V}_{K'}^h = \{(w'_l, \hat{\xi}'_l) | l = 1, 2, \dots, K'\}$ , is different from that for  $g$ ,  $\mathcal{V}_K^g = \{(w_k, \hat{\xi}_k) | k = 1, 2, \dots, K\}$ , the discrete velocities in the two sets generally do not coincide with each other, and subsequently the term  $R^z$  in Eq. (7b) cannot be represented by its discrete versions straightforwardly. To overcome this inconsistency, we note that only the zeroth- and first-order velocity moments of  $R^z$  is required in the Chapman-Enskog analysis of the kinetic model (7), and therefore we can replace it with its first-order Hermite polynomial expansion,

$$R^z \approx \omega(\hat{\xi})(\mathbf{P} - \rho \mathbf{I}) : \hat{\xi} \hat{\mathbf{u}}, \quad (30)$$

where  $\mathbf{I}$  is the second-order unity tensor. It can be seen that  $g$  does not appear explicitly in the kinetic equation for  $h$  now, and then the discrete velocity version for  $h$  can be written as

$$\partial_t h_l + \hat{\xi}'_l \cdot \nabla h_l = -\frac{1}{\tau_h} (h_l - h_l^{(eq)}) + \frac{1}{\tau_{hg}} R_l^z, \quad (31)$$

where  $h_l = w'_l h(\hat{\xi}'_l) / \omega'(\hat{\xi}'_l)$ , and the discrete equilibrium is given by

$$h_l^{(eq)} = w'_l p [\hat{\xi}'_l \cdot \hat{\mathbf{u}} + (\hat{\xi}'_l \cdot \hat{\mathbf{u}})^2 - \hat{u}^2 + \frac{1}{2}\theta(\hat{\xi}'_l^2 - D)] + E g_{2,l}^{(eq)}, \quad (32)$$

with

$$g_{2,l}^{(eq)} = w'_l \rho \left\{ 1 + \hat{\xi}'_l \cdot \hat{\mathbf{u}} + \frac{1}{2} [(\hat{\xi}'_l \cdot \hat{\mathbf{u}})^2 - \hat{u}^2 + (\theta - 1)(\hat{\xi}'_l^2 - D)] \right\}, \quad (33)$$

while the corresponding discrete version of  $R^z$  is given by

$$R_l^z = w'_l (\mathbf{P} - \rho \mathbf{I}) : \hat{\xi}'_l \hat{\mathbf{u}}. \quad (34)$$

The total energy and heat flux are obtained as

$$\rho E = \sum_l h_l, \quad \mathbf{q} = \sum_l \mathbf{c}'_l h_l - \mathbf{P} \cdot \mathbf{u}, \quad (35)$$

where the pressure tensor  $\mathbf{P}$  is obtained from  $g_k$  as before, and  $\mathbf{c}'_l = \hat{\xi}'_l - \mathbf{u}$ .

It should be noted that the Hermite approximation of  $R^z$  given by Eq. (30) can also be employed if the DVS's for both  $g$  and  $h$  are identical. Therefore, this formulation is general for designing DVKE consistent with the compressible Navier-Stokes equations. In the present study, we will adopt this formulation to develop the DUGKS for continuum compressible flows. However, the original formulation given by

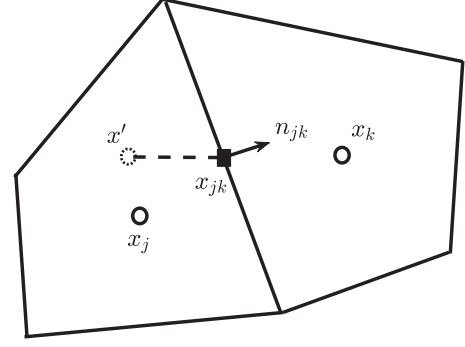


FIG. 1. Schematic of two neighboring cells  $V_j$  and  $V_k$  centered at  $\mathbf{x}_j$  and  $\mathbf{x}_k$ , respectively.  $\mathbf{x}_{jk}$  is the center of cell interface, and  $\mathbf{n}_{jk}$  is the outward norm unit vector of cell  $V_j$  at  $\mathbf{x}_{jk}$ .

Eq. (10) should be adopted to design numerical schemes for noncontinuum flows in order to capture the nonequilibrium effects beyond the Navier-Stokes hydrodynamics, as shown in [55].

*Remark 1.* We note that the Hermite expansions  $g_3^{(eq)}$  and  $h_2^{(eq)}$  have also been employed in a LBE [31]. However, the DVS's were chosen as the standard on-lattice ones corresponding to the fifth-degree Hermite quadratures. Consequently, the velocity moments requirements (14) are not fully satisfied. In order to reproduce the correct hydrodynamic equations, some carefully designed correction terms must be introduced into the LBE.

*Remark 2.* The total-energy kinetic model was also employed in a DUGKS for multiscale flows [55], where the discrete velocities are not specified for the compressible Navier-Stokes equations and therefore are not optimized.

### III. DUGKS FOR THE TOTAL ENERGY MODEL

The DVKE's (22) and (25) [or (31)] exhibit the same formulation,

$$\partial_t \phi_i + \hat{\xi}_i \cdot \nabla \phi_i = Q_i^\phi, \quad (36)$$

where  $\phi = g$  or  $h$ , and  $Q_i^\phi$  is the generalized collision term,

$$Q_i^\phi = \begin{cases} -\frac{1}{\tau_g} [g_i - g_i^{(eq)}], & \phi = g, \\ -\frac{1}{\tau_h} [h_i - h_i^{(eq)}] + \frac{1}{\tau_{hg}} R_i^z, & \phi = h, \end{cases} \quad (37)$$

with  $R_i^z$  given by Eq. (26) or Eq. (34), depending on whether the DVS for  $h$  is the same as that for  $g$ . It is easy to verify that  $Q_i^\phi$  is conservative, namely,

$$\sum_i Q_i^g = 0, \quad \sum_i \hat{\xi}_i Q_i^g = 0, \quad \sum_l Q_l^h = 0. \quad (38)$$

We now present the DUGKS to solve Eq. (36), which is a finite-volume discretization of the kinetic equation. The physical space is first discretized into a set of cells (or control volumes)  $V_j$  centered at  $\mathbf{x}_j$ , where  $j$  is the index number of the cell (see Fig. 1). The average of a quantity  $\varphi(\mathbf{x}, t)$  in  $V_j$  is

denoted by

$$\varphi_{i,j}(t) = \frac{1}{|V_j|} \int_{V_j} \varphi_i(\mathbf{x}, t) d\mathbf{x}, \quad (39)$$

where  $|V_j|$  is the volume of cell  $V_j$ . Then integrating Eq. (36) over cell  $V_j$  from  $t_n$  to  $t_{n+1}$  leads to

$$\phi_{i,j}^{n+1} - \phi_{i,j}^n + \frac{\Delta t}{|V_j|} F_{i,j}^{\phi,n+1/2} = \frac{\Delta t}{2} [Q_{i,j}^{\phi,n+1} + Q_{i,j}^{\phi,n}], \quad (40)$$

where the midpoint rule for the time integration of the convection term and trapezoidal rule for the collision term are used, respectively. The interface flux at the half time step,  $F_{i,j}^{\phi,n+1/2}$ , is evaluated via the midpoint rule for the surface integration,

$$\begin{aligned} F_{i,j}^{\phi,n+1/2} &= \int_{\partial V_j} (\boldsymbol{\xi}_i \cdot \mathbf{n}) \phi_i^{n+1/2}(\mathbf{x}) dS \\ &= \sum_k (\boldsymbol{\xi}_i \cdot \mathbf{n}_{jk}) \phi_i^{n+1/2}(\mathbf{x}_{jk}) S_{jk}, \end{aligned} \quad (41)$$

where  $\phi_i^{n+1/2}(\mathbf{x}) = \phi_i(\mathbf{x}, t_n + s)$  with  $s = \Delta t/2$ ,  $\partial V_j$  is the surface of cell  $V_j$  and  $\mathbf{n}$  is the outward unit vector normal to the surface, and  $S_{jk}$  is the surface area of the interface between cell  $V_j$  and neighboring cell  $V_k$ .

In order to evaluate the flux, the distribution function on cell interface at half time step,  $\phi_i^{n+1/2}(\mathbf{x}_{jk})$ , should be first reconstructed from the cell-averaged distribution functions. The most typical feature of DUGKS that distinguishes it from other kinetic schemes is that the reconstruction is based on the discrete characteristic solution of the kinetic equation. Specifically,  $\phi_i^{n+1/2}(\mathbf{x}_{jk})$  is obtained by integrating the kinetic equation along the characteristic line from  $\mathbf{x}' = \mathbf{x}_{jk} - \boldsymbol{\xi}_i s$  to  $\mathbf{x}_{jk}$  with a half time step,

$$\phi_i(\mathbf{x}_{jk}, t_n + s) - \phi_i(\mathbf{x}', t_n) = \frac{s}{2} [Q_i^\phi(\mathbf{x}_{jk}, t_n + s) + Q_i^\phi(\mathbf{x}', t_n)], \quad (42)$$

where the trapezoidal rule is again used for the collision term.

Equations (40) and (42) define the general formulation of DUGKS. It is noted that both are semi-implicit due to the trapezoidal rule used for the collision term. Different strategies can be employed to remove the implicitness [5]. Here we adopt the method in the original DUGKS [5]. Specifically, we first introduce the following four distribution functions,

$$\begin{aligned} \tilde{\phi}_i &= \phi_i - \frac{\Delta t}{2} Q_i^\phi, & \tilde{\phi}_i^+ &= \phi_i + \frac{\Delta t}{2} Q_i^\phi, \\ \bar{\phi}_i &= \phi_i - \frac{\Delta t}{4} Q_i^\phi, & \bar{\phi}_i^+ &= \phi_i + \frac{\Delta t}{4} Q_i^\phi. \end{aligned} \quad (43)$$

Then Eqs. (40) and (42) can be implemented explicitly,

$$\tilde{\phi}_{i,j}^{n+1} = \tilde{\phi}_{i,j}^{+,n} - \frac{\Delta t}{|V_j|} F_{i,j}^{\phi,n+1/2}, \quad (44)$$

$$\bar{\phi}_i^{n+1/2}(\mathbf{x}_{jk}) = \bar{\phi}_i^{+,n}(\mathbf{x}'). \quad (45)$$

The auxiliary distribution function  $\bar{\phi}_i^+(\mathbf{x}', t_n)$  can be reconstructed from the cell-averaged distribution functions  $\bar{\phi}_i^+(t_n)$  of neighboring cells. For smooth flows, this can be achieved

by assuming  $\bar{\phi}_i^+(\mathbf{x})$  is linear around  $\mathbf{x}_{jk}$ ,

$$\bar{\phi}_i^+(\mathbf{x}', t_n) = \bar{\phi}_i^+(\mathbf{x}_{jk}, t_n) - s \boldsymbol{\xi}_i \cdot \boldsymbol{\sigma}_i(\mathbf{x}_{jk}), \quad (46)$$

where the interface value  $\bar{\phi}_i^+(\mathbf{x}_{jk}, t_n)$  and the slope  $\boldsymbol{\sigma}_i(\mathbf{x}_{jk})$  can be approximated by interpolations. For flows with discontinuities,  $\bar{\phi}_i^+(\mathbf{x})$  is assumed to be piecewise linear in each cell, and  $\bar{\phi}_i^+(\mathbf{x}', t_n)$  is reconstructed as

$$\begin{aligned} \bar{\phi}_i^+(\mathbf{x}', t_n) &= \begin{cases} \bar{\phi}_i^+(\mathbf{x}_j, t_n) + (\mathbf{x}_{jk} - \boldsymbol{\xi}_i s - \mathbf{x}_j) \boldsymbol{\sigma}_{i,j}, & \boldsymbol{\xi}_i \cdot \mathbf{n}_{jk} > 0, \\ \bar{\phi}_i^+(\mathbf{x}_k, t_n) + (\mathbf{x}_{jk} - \boldsymbol{\xi}_i s - \mathbf{x}_k) \boldsymbol{\sigma}_{i,k}, & \boldsymbol{\xi}_i \cdot \mathbf{n}_{jk} < 0, \end{cases} \end{aligned} \quad (47)$$

where  $\boldsymbol{\sigma}_{i,\alpha}$  is the slope of  $\bar{\phi}_i^+(t_n)$  in cell  $V_\alpha$  ( $\alpha = j$  or  $k$ ), which can be determined from the cell-averaged values. In the present study, two approaches are adopted to calculate the slope, i.e., the van Leer limiter [63] and a fifth-order weighted essentially nonoscillatory (WENO) interpolation [64]. In the one-dimensional case, the slope of a variable  $\psi$  in cell  $V_j = [x_{j-1/2}, x_{j+1/2}]$  determined by the van Leer limiter is

$$\sigma_j(\psi) = [\text{sgn}(s_1) + \text{sgn}(s_2)] \frac{|s_1||s_2|}{|s_1| + |s_2|}, \quad (48)$$

where

$$s_1 = \frac{\psi_j - \psi_{j-1}}{x_j - x_{j-1}}, \quad s_2 = \frac{\psi_{j+1} - \psi_j}{x_{j+1} - x_j}, \quad (49)$$

with  $j$  being the label of the cell and  $x_j$  is the center of cell  $V_j$ . The fifth-order WENO interpolation is a bit more complex. For the one-dimensional case, the slope in cell  $V_j$  is given by

$$\sigma_j(\psi) = \frac{\psi_{j+1/2} - \psi_{j-1/2}}{x_{j+1/2} - x_{j-1/2}}, \quad (50)$$

where  $\psi_{j\pm 1/2}$  is a convex combination of the interpolated values  $\psi_{j\pm 1/2}^{(k)}$ ,

$$\psi_{j\pm 1/2} = \sum_{k=0}^2 \omega_k \psi_{j\pm 1/2}^{(k)}, \quad (51)$$

where the weights  $\omega_k$  are chosen based on certain smoothness indicators, and the interpolated values are given by

$$\psi_{j+1/2}^{(k)} = \sum_{l=0}^2 c_{kl} \psi_{j-k+l}, \quad (52)$$

with  $c_{kl}$  being the Lagrangian interpolation coefficients dependent on the  $k$ th three-point stencil. The detailed expressions of the weights and smooth indicators can be found in Ref. [64]. In our simulations, multidimensional Cartesian meshes are employed, and the slope in each direction is calculated separately following the above procedure.

Once  $\bar{\phi}_i(\mathbf{x}', t_n)$  is obtained,  $\bar{\phi}_i^{n+1/2}(\mathbf{x}_{jk})$  can be calculated from Eq. (45), and the conservative hydrodynamic variables (density, velocity, and energy) at the cell interface  $\mathbf{x}_{jk}$  can be obtained,

$$\begin{aligned} \rho^{n+1/2} &= \sum_i \bar{g}_i^{n+1/2}, & (\rho \mathbf{u})^{n+1/2} &= \sum_i \boldsymbol{\xi}_i \bar{g}_i^{n+1/2}, \\ (\rho E)^{n+1/2} &= \sum_l \bar{h}_l^{n+1/2}, \end{aligned} \quad (53)$$

and the pressure tensor is computed by

$$\mathbf{P}^{n+1/2} = \frac{4\tau_g}{4\tau_g + \Delta t} \sum_i \mathbf{c}_i \mathbf{c}_i \tilde{g}_i^{n+1/2} + \frac{\Delta t}{4\tau_g + \Delta t} p^{n+1/2} \mathbf{I}, \quad (54)$$

where we have used the conservative property of the collision terms, Eq. (38). Then, the original distribution function  $\phi$  at the cell interface can be obtained from  $\tilde{\phi}$  according to their relationship given in Eq. (43),

$$\begin{aligned} \phi_i^{n+1/2} &= \frac{4\tau_\phi}{4\tau_\phi + \Delta t} \tilde{\phi}_i^{n+1/2} \\ &+ \frac{\Delta t}{4\tau_\phi + \Delta t} [\phi_i^{(eq),n+1/2} + S_i^{\phi,n+1/2}], \end{aligned} \quad (55)$$

where  $S_i^g = 0$  and  $S_i^h = (1 - Pr^{-1})R_i^z$ . Then the interface flux  $F_{i,j}^{\phi,n+1/2}$  can be determined based on Eq. (41).

In practical simulations, the transformed distribution function  $\tilde{\phi}$  is tracked instead of the original distribution function  $\phi$ , which is easier to implement. In this case,  $\tilde{\phi}_i^+$  and  $\tilde{\phi}_i^-$  are computed as

$$\tilde{\phi}_i^+ = \frac{4\tau - \Delta t}{4\tau + 2\Delta t} \tilde{\phi}_i + \frac{3\Delta t}{4\tau + 2\Delta t} \phi_i^{(eq)}, \quad \tilde{\phi}_i^- = \frac{4}{3} \tilde{\phi}_i^+ - \frac{1}{3} \tilde{\phi}_i. \quad (56)$$

Then the DUGKS can be realized following Eq. (44) with the aids of Eqs. (46) [or (47)], (55), and (56). The hydrodynamic variables can also be computed from  $\tilde{\phi}_i$ ,

$$\rho = \sum_i \tilde{g}_k, \quad \rho \mathbf{u} = \sum_k \tilde{\xi}_k \tilde{g}_k, \quad (57)$$

$$\begin{aligned} \mathbf{P} &= \frac{2\tau_g}{2\tau_g + \Delta t} \sum_k \mathbf{c}_k \mathbf{c}_k \tilde{g}_k + \frac{\Delta t}{2\tau_g + \Delta t} p \mathbf{I}, \\ \rho E &= \sum_l \tilde{h}_l, \quad \mathbf{q} = \sum_l \mathbf{c}'_l \tilde{h}_l - \mathbf{P} \cdot \mathbf{u}, \end{aligned} \quad (58)$$

Finally, the time step  $\Delta t$  is determined by the CFL condition,

$$\Delta t = \frac{\beta \Delta x}{|\tilde{\xi}|_{\max} + |\mathbf{u}|_{\max} + c_{\max}}, \quad (59)$$

where  $0 < \beta \leq \beta_0$  is the CFL number with  $\beta_0$  being a constant,  $|\tilde{\xi}|_{\max}$  is the maximum values of the discrete velocities in the two DVS's for the distribution functions  $g$  and  $h$ ,  $|\mathbf{u}|_{\max}$  is the maximum velocity, and  $c_{\max}$  is the maximum sound speed. Note that the CFL condition given by Eq. (59) is more restrictive than that determined solely by the maximum discrete velocity  $|\tilde{\xi}|_{\max}$ . This is reasonable since the present DUGKS preserves the Navier-Stokes equations in the continuum limit,

for which the CFL condition should also depend on the macroscopic flow velocity and sound speed [4].

We remark that it is a nontrivial task to make a rigorous analysis of numerical instability of the proposed DUGKS. However, several important influential factors can be identified. First, the positiveness of the (transformed) distribution functions  $\tilde{g}_i$  and  $\tilde{h}_l$  cannot be preserved at large Ma due to the use of Hermite expansions of the equilibrium distribution functions. This positiveness is a sufficient (but not necessary) condition for stable computation. Actually, the transformed distribution functions in the simulation are rather mathematical constructs and not exactly identical to the physical ones of the kinetic equation. Therefore, the computation can be still stable even some of the transformed distribution functions take negative values in the evolution. Second, it is noted that although the DVSs used for  $g$  and  $h$  satisfy the moment requirements given by Eq. (14), higher-order moments may not be satisfied, and an upper limit of Mach number for valid and stable simulations exists for a given DVS [29]. Therefore, a DVS of high-order quadrature is preferred for simulating high Mach number flows. Third, the ratio of time step to relaxation time,  $r = \Delta t/\tau$ , also affects the numerical stability. As shown by Eq. (56), in the time evolution the computation  $\tilde{\phi}_i^+ = \tilde{\phi} + [2r/(2+r)](\tilde{\phi}_i - \phi_i^{(eq)})$  becomes an over relaxation process as  $r > 2$ , which is similar to the collision process of standard LBE. Therefore, numerical instability may occur in the simulation of flows with small viscosity or large Reynolds number. The numerical stability can be improved by replacing the discrete BGK collision operator with some advanced collision models such as multiple relaxation model [65], cascaded moment model [66], regularization model [67], cumulant model [68], and numerical equilibria [23], as used in LBE. Finally, we note that the flux construction has a significant influence on numerical stability. Generally, a reconstruction with upwind properties exhibits good numerical stability.

## IV. NUMERICAL TESTS

The performance of the proposed DUGKS based on the total-energy kinetic model will be verified by simulating a 2D Riemann problem and the 3D Taylor-Green decaying flows at different Mach numbers. In the simulations, the van Leer limiter is employed in the reconstruction of interface flux, and the CFL number is set to be 0.5. The gas constant  $R$  is set to be 1.0.

### A. 2D Riemann problem

We first consider one two-dimensional Riemann problem with constant initial data in each quadrant, i.e., Configuration 12 listed in Ref. [69],

$$(\rho, u, v, p) = \begin{cases} (\rho_1, u_1, v_1, p_1) = (0.5313, 0, 0, 0.4), & x > 0.5, \quad y > 0.5, \\ (\rho_2, u_2, v_2, p_2) = (1, 0.7276, 0, 1), & x \leq 0.5, \quad y > 0.5, \\ (\rho_3, u_3, v_3, p_3) = (0.8, 0, 0, 1), & x \leq 0.5, \quad y \leq 0.5, \\ (\rho_4, u_4, v_4, p_4) = (1, 0, 0.7276, 1), & x > 0.5, \quad y \leq 0.5, \end{cases} \quad (60)$$



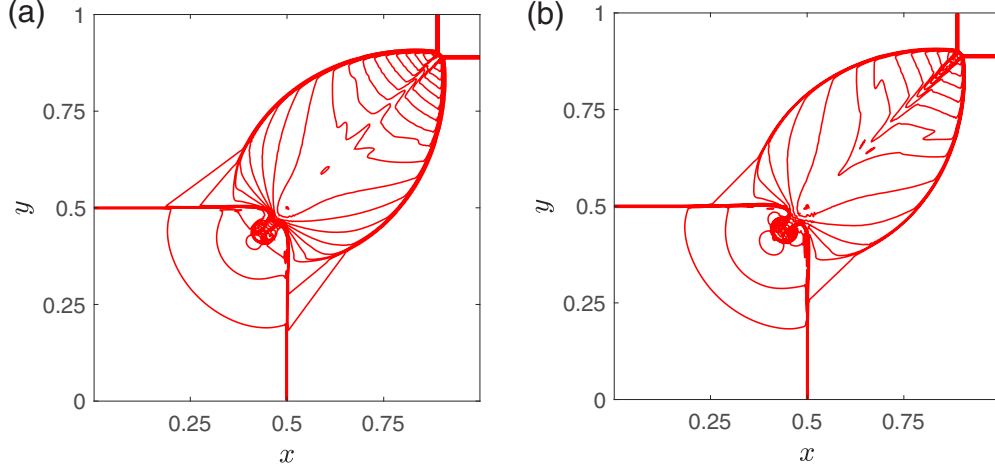


FIG. 2. The density (a) and temperature (b) fields of the 2D Riemann problem at  $t = 0.25$ . Mesh size:  $400 \times 400$ .

where  $\mathbf{u} = (u, v)$  is the flow velocity. The Prandtl number and heat capacity ratio are set to be  $\text{Pr} = 2/3$  and  $\gamma = 1.4$ , respectively. The reference density, temperature, and pressure are chosen to be  $\rho_0 = 1.0$ ,  $T_0 = 1.0$ , and  $p_0 = \rho_0 RT_0 = 1.0$ , respectively. The local viscosity is determined by  $\mu = \mu_0 (T/T_0)^w$  with  $w = 0.5$ , where  $\mu_0 = 10^{-7}$  is the reference viscosity at the reference temperature  $T_0$ . A  $400 \times 400$  uniform mesh is employed, and no-flux boundary conditions are applied to the four boundaries, i.e.,  $\partial_n f = 0$ , where  $\mathbf{n}$  is the outward unit normal vector.

The D2V12-A7 and D2V6-A4 are applied to discretize the velocity spaces of  $g$  and  $h$ , respectively. It is noted that the reference mean-free path  $\lambda_0 = (\mu_0/p_0)\sqrt{\pi RT_0/2} \approx 1.253 \times 10^{-7}$ , and the reference relaxation time  $\tau_0 = \mu_0/p_0 = 10^{-7}$ , while the mesh cell size  $\Delta x = 2.5 \times 10^{-3} \gg \lambda_0$ , and the time step  $\Delta t$  determined by the CFL condition (59) is at the order of  $10^{-4}$ , which is also much larger than the relaxation time. Figure 2 shows the 31 equally spaced contours of density ( $\rho \in [0.54, 1.7]$ ) and temperature ( $T \in [0.76, 1.39]$ ) at  $t = 0.25$ . It can be seen that the structures are consistent with previous studies [5,69].

### B. 3D Taylor-Green vortex

We now simulate the 3D Taylor-Green vortex in a periodic box  $[0, 2\pi L]^3$ , which undergoes creation of small scales due to vortex stretching and initial distribution of vorticity. It is noted that this flow was also simulated by a semi-Lagrangian LBE recently [38]. The initial velocity  $\mathbf{u} = (u, v, w)$ , pressure  $p$ , temperature  $T$ , and density  $\rho$ , are given by

$$\begin{aligned} u &= u_0 \sin x' \cos y' \cos z', \\ v &= -u_0 \cos x' \sin y' \cos z', \\ w &= 0, \\ p &= p_0 + \frac{\rho_0 u_0^2}{16} [\cos(2x') + \cos(2y')] [\cos(2z') + 2], \\ T &= T_0, \quad \rho = p/RT_0, \end{aligned} \quad (61)$$

where  $(x', y', z') = (x, y, z)/L$ , and the variables with subscript “0” represent their constant reference values. The initial

Mach and Reynolds numbers are given by  $\text{Ma} = u_0/\sqrt{\gamma RT_0}$  and  $\text{Re} = \rho_0 L u_0/\mu_0$ , respectively, where  $\rho_0 = p_0/RT_0$  and  $\mu_0$  are the reference density and dynamic viscosity, respectively. The local viscosity generally changes with temperature, and here Sutherland’s law is employed,

$$\mu = \mu_0 \frac{1.4042(T/T_0)^{1.5}}{T/T_0 + 0.40417}. \quad (62)$$

In our simulations, we choose  $L = 1.0$ ,  $T_0 = 1.0$ ,  $u_0 = 1.0$ , and  $\rho_0 = 1.0$ , then  $R$  and  $\mu_0$  are determined from the given Mach and Reynolds numbers. The heat capacity ratio is set to be  $\gamma = 1.4$ , and the Prandtl number is  $\text{Pr} = 0.71$ .

The D3V27-A7 ( $\{(w_i, \xi_i) | i = 1, 2, \dots, 27\}$ ) and D3V13-A5 ( $\{(w'_l, \xi'_l) | l = 1, 2, \dots, 13\}$ ) listed in Table I are employed to discretize the velocity space of  $g$  and  $h$ , respectively. The distribution functions  $g_i$  and  $h_l$  are initialized by their first-order Chapman-Enskog approximations, namely,  $g_i = g_i^{(eq)} + g_i^{(neq)}$  and  $h_l = h_l^{(eq)} + h_l^{(neq)}$ , where the nonequilibrium parts  $g^{(neq)}$  and  $h^{(neq)}$  depend on the viscous stress and heat flux,

$$g_i^{(neq)} = -w_i \frac{\boldsymbol{\tau} : (\xi_i \xi_i - RT_0 \mathbf{I})}{2(RT_0)^2}, \quad (63a)$$

$$h_l^{(neq)} = -w'_l \frac{(\kappa \nabla T + \boldsymbol{\tau} \cdot \mathbf{u}) \cdot \xi'_l}{RT_0}, \quad (63b)$$

where the viscous stress  $\boldsymbol{\tau}$  and gradient of  $T$  are calculated from the initial field given by Eq. (61) analytically.

In our tests, the Reynolds number is set to be 1600, as considered in [70]. Four Mach numbers are chosen,  $\text{Ma} = 0.1, 1.0$ , and  $1.25$ , corresponding to subsonic, transonic, and supersonic flow regimes, respectively. We note that the computation using the D3V27-A7 with the upper signs (Group I) listed in Table I is stable for all cases, but becomes unstable when using the other group (Group II) for the case of  $\text{Ma} = 1.25$ . This may be due to the less numerical dissipation introduced by the Group II DVS, as shown in Appendix. Therefore, in the following we give only the results using the D3V27-A7 of Group I.

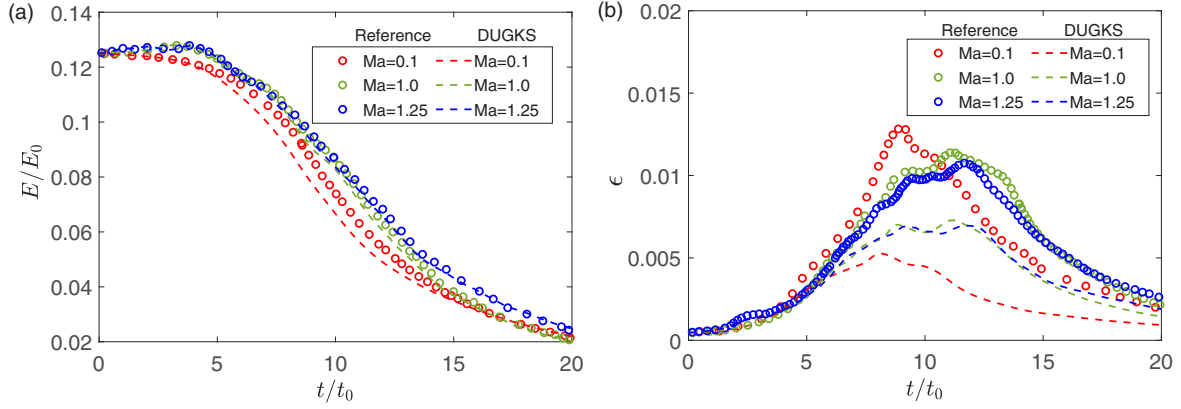


FIG. 3. Time histories of the total kinetic energy (a) and dissipation rates (b) predicted by the present DUGKS with the van Leer reconstruction at different Mach numbers on a mesh of size  $256^3$ . The kinetic energy and time are normalized by  $E_0 = \rho_0 u_0^2$  and  $t_0 = L/u_0$ , respectively. The reference data are taken from Refs. [70] and [71]: data for  $Ma = 0.1$  are the spectral solution on a  $512^3$  mesh, data for  $Ma = 1.0$  are the sixth-order TENO solution on a  $1024^3$  mesh; data for  $Ma = 1.25$  are the sixth-order TENO solution on a  $768^3$  mesh.

To quantify the comparison, we measure the nondimensional volume-averaged kinetic energy  $E$  and total viscous dissipation rate  $\epsilon$ , which are defined by

$$E = \frac{1}{\rho_0 u_0^2 V} \int_V \frac{1}{2} \rho \mathbf{u}^2 dx, \quad (64a)$$

$$\epsilon = \epsilon_s + \epsilon_d = \frac{1}{\text{Re} \rho_0 u_0^2 \mu_0 V} \int_V \mu (\nabla \times \mathbf{u})^2 dx + \frac{1}{\text{Re} \rho_0 u_0^2 \mu_0 V} \int_V \left( \mu_b + \frac{4}{3} \mu \right) (\nabla \cdot \mathbf{u})^2 dx, \quad (64b)$$

where  $V$  is the volume of the computational domain,  $\epsilon_s$  and  $\epsilon_d$  represent the solenoidal (enstrophy) dissipation rate and dilatational one, respectively. For the low Mach case, the contribution of  $\epsilon_d$  to the total dissipation is negligible, and  $\epsilon_s$  is a close approximation of  $\epsilon$ .

In Fig. 3 the time histories of the kinetic energies and viscous dissipation rates at different Mach numbers predicted by the present DUGKS with the van Leer reconstruction (DUGKS-vL) are presented. The reference data from Refs. [70] are also included, which were obtained by the spectral method or the sixth-order Targeted Essentially Non-Oscillatory (TENO6) on fine meshes. It can be observed from Fig. 3(a) that the DUGKS-vL can predict the decaying process of the kinetic energy at  $Ma = 0.1$ , and the nonmonotonic changes at  $Ma = 1.0$  and  $1.25$  due to the compressible effects. However, it is noted that the kinetic energy predicted by the DUGKS-vL decays faster than the reference data in each case, suggesting that the large numerical dissipation in DUGKS-vL. This is more evident from Fig. 3(b), where the DUGKS-vL underestimates the viscous dissipation rates compared to the reference data, suggesting the small-scale flow structures are not resolved.

The insufficient capability in capturing the small-scale dynamics of DUGKS-vL is expected, since the limiter introduces additional numerical dissipation even in smooth region. To see this more clearly, we rerun the simulation for the case of  $Ma = 0.1$  by turning off the limiter, where the compressibility can be ignored and no discontinuity appears in the flow. The kinetic energy and dissipation rate

are shown in Fig. 4. It can be clearly seen that the results without the limiter are improved in comparison with those with the van Leer limiter. It should be noted that, however, the DUGKS without the van Leer limiter will become unstable with the increase of compressibility at large Mach numbers.

In the framework of the present DUGKS for compressible flows, the accuracy can also be partially improved by employing high-order interpolations in the flux reconstruction. As an example, the DUGKS with the fifth-order weighted essentially nonoscillatory flux construction (denoted by DUGKS-WENO) is also used to simulate this Taylor-Green vortex flow. It is noted that the overall spatial accuracy is still second-order, since the trapezoidal rule and piecewise linear assumption are still employed in Eqs. (42) and (47). The kinetic energies and viscous dissipation rates over time predicted by DUGKS-WENO for  $Ma = 0.1$  and  $1.0$  are shown in Fig. 5, from which clear improvements can be observed in comparison with the results of DUGKS-vL. We note that this DUGKS-WENO becomes unstable at  $Ma = 1.25$  with the  $256^3$  mesh. Therefore, further work is needed to design a low-dissipation and robust DUGKS for compressible turbulence [70].

Simulations with a finer mesh of size  $512^3$  are also conducted. The kinetic energies and viscous dissipation rates at  $Ma = 1.0$  are shown in Fig. 6. The time histories of kinetic energy predicted by DUGKS-vL and DUGKS WENO are both in excellent agreement with the reference data. For the dissipation rate, the result of the DUGKS-WENO is quite satisfying, but clear deviations can still be observed for the result of DUGKS-vL, although much improvement is gained in comparison with the results on the  $256^3$  mesh. We remark that with this  $512^3$  mesh, both DUGKS-vL and DUGKS-WENO are unstable for  $Ma = 1.25$ , meaning that increasing the mesh resolution does not necessarily increase the numerical stability. This may be because, while the large gradients can be better captured with a finer mesh, the numerical dissipation also becomes smaller. The competition between these two effects may lead to numerical instability, particularly for high Mach flows where large numerical dissipation is required to capture local discontinuities.

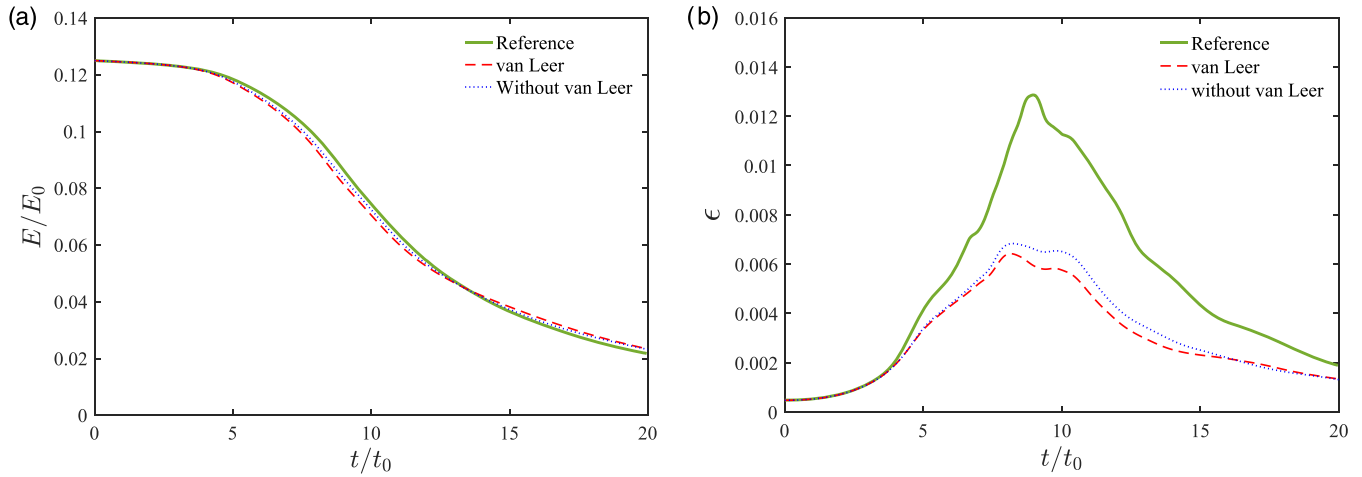


FIG. 4. Same as Fig. 3 but for the results at  $Ma = 0.1$  with and without the van Leer reconstruction.

Finally, it is interesting to notice from Figs. 3 and 5 that both kinetic energy and dissipation rate predicted by the present DUGKS at  $Ma = 0.1$  deviate large from the reference data relatively, whereas the results at  $Ma = 1.0$  and/or 1.25 are far better. This interesting phenomenon may be due to the strength of compressibility effects at different Mach numbers. At  $Ma = 0.1$ , the flow is smooth but the additional numerical dissipation introduced by the van Leer limiter and the WENO interpolation degenerates the accuracy at local smooth extremes. On the other hand, local discontinuities appear in the flow field at  $Ma = 1.0$  and 1.25, and the DUGKS with both flux reconstruction techniques can capture the discontinuities such that the whole flow field can be well resolved. This phenomenon may be also related to the effects of the numerical dissipation on acoustic and shear waves, which should be investigated further.

V. SUMMARY

In the present work, an efficient DUGKS algorithm for simulating continuum compressible flows is presented. The DUGKS is constructed based on the total energy kinetic model [20], which has a flexible Prandtl number and specific

heat ratio. The density and energy equilibrium distribution functions,  $g$  and  $h$ , are represented by their Hermite polynomial expansions up to third and second orders, respectively, which are shown to be sufficient to recover the compressible Navier-Stokes equations. Consequently, the corresponding discrete velocity sets for the two populations can be determined by the Gauss-Hermite quadrature rules with sixth and fourth degrees of precision, respectively. One choice is using the D2V12-A7 for  $g$  and D2V6-A4 for  $h$  for 2D flows, and using D3V27-A7 for  $g$  and D3V13-A5 for  $h$  for 3D flows. In comparison with previous DUGKS with a DVS determined from the Gauss-Hermite quadratures of at least ninth degree, the computational loads can be much reduced.

A 2D Riemann problem and the 3D Taylor-Green vortex at  $Re = 1600$  are simulated. The results demonstrate the good shock capturing property of the present DUGKS. The results for the Taylor-Green vortex demonstrate that the DUGKS with the van Leer is more dissipative for resolving small-scale structures. This can be partially improved by employing high-order reconstruction methods. Another critical problem of the present DUGKS is the numerical instability for large Mach numbers, which may be due to a number of factors. This may be improved from different approaches, such as

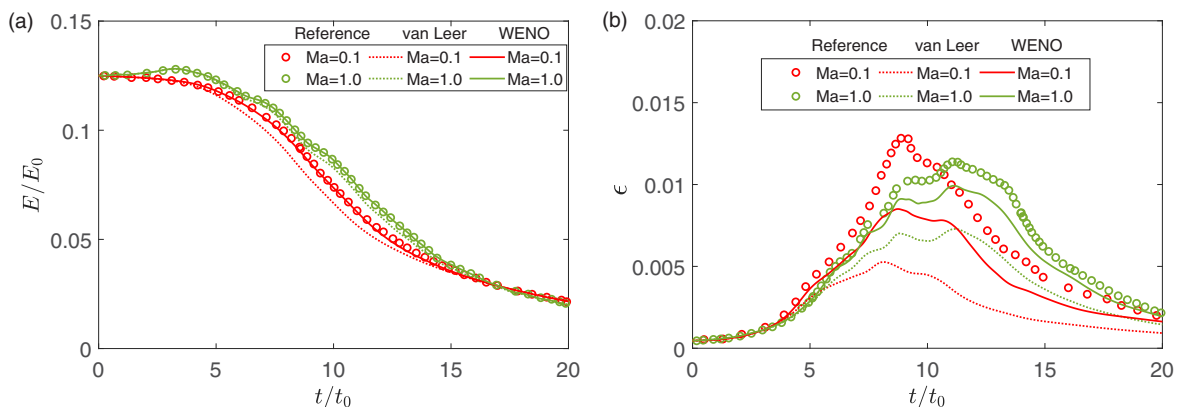


FIG. 5. Time histories of the total kinetic energy (a) and dissipation rates (b) predicted by the present DUGKS with the van Leer and WENO reconstruction at different Mach numbers on a mesh of size  $256^3$ .

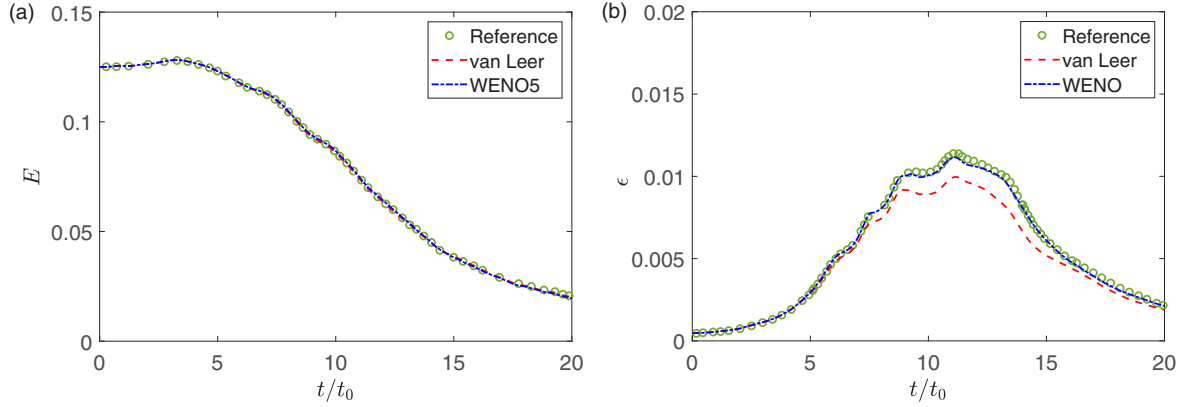


FIG. 6. Time histories of the total kinetic energy (a) and dissipation rates (b) predicted by the present DUGKS with the van Leer and WENO reconstruction at  $Ma = 1.0$  on a mesh of size  $512^3$ .

replacing the BGK collision operator with more advanced collision models. Particularly, the numerical equilibria approach [23] can ensure the positiveness of the equilibrium distribution functions. However, it should be noted that the computation is expensive in that the numerical equilibria are computed through a root-finding approach. Our future work will focus on developing robust and low-dissipation DUGKS for compressible turbulent flows based on the total energy kinetic model as employed in the present work.

Finally, we remark that recently we have simulated the compressible decaying homogeneous isotropic turbulence at low and moderate turbulent Mach numbers using a reformulation of the present DUGKS with a fifth-order WENO flux reconstruction and a different source term, which shows good predictions of the different transient stages from the initial random flow field to the developed turbulence [72].

**ACKNOWLEDGMENTS**

Z.L.G. acknowledges the support by the National Natural Science Foundation of China (51836003), and part of the

work was carried out during his visit to Southern University of Science and Technology. L.P.W. was supported by the National Natural Science Foundation of China (11988102 and 91852205). Computing resources are provided by the Center for Computational Science and Engineering of Southern University of Science and Technology.

**APPENDIX: COMPARISON OF THE TWO DVS GROUPS OF D3V27-A7**

It is noted that the DUGKS with the D3V27-A7 of Group II becomes unstable in the simulation of the Taylor-Green vortex, while that of Group I is stable. This can be attributed to the less numerical dissipation of Group II. To confirm this point, we compare here the time histories of the enstrophy at  $Ma = 0.1$  and  $1.0$ . In the computation, the fifth-order WENO is employed in the flux reconstruction, and a uniform mesh of size  $256^3$  is used. The results are shown in Fig. 7. It can be observed that the D3V27-A7 of Group II does lead to less numerical dissipation than Group I. This can partially explain the numerical instability when using the DVS of Group II.

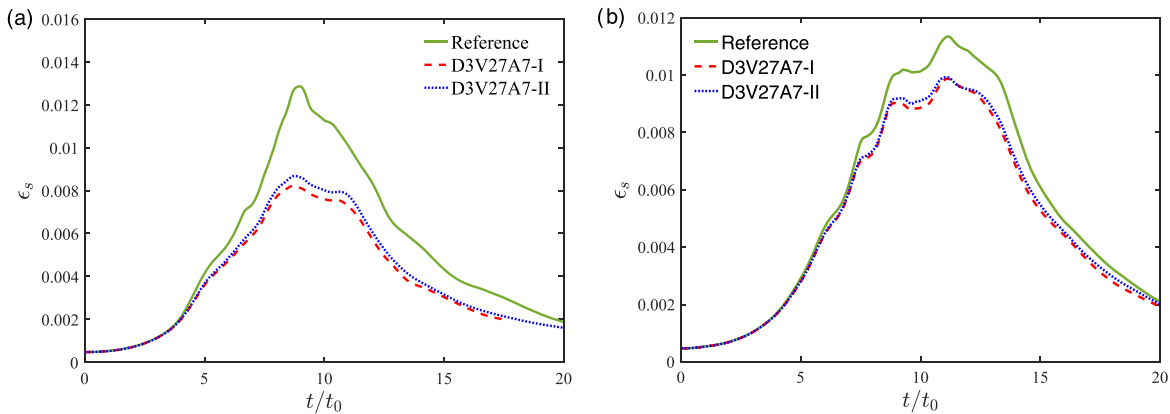


FIG. 7. Time histories of the enstrophy dissipation rates with the two D3V27-A7 DVS's at  $Ma = 0.1$  (a) and  $1.0$  (b).

- [1] K. Xu, *J. Comput. Phys.* **171**, 289 (2001).
- [2] J.-Y. Yang and J. C. Huang, *J. Comput. Phys.* **120**, 323 (1995).
- [3] J. W. Hu and X. X. Zhang, *J. Sci. Comput.* **73**, 797 (2017).
- [4] K. Xu and J.-C. Huang, *J. Comput. Phys.* **229**, 7747 (2010).
- [5] Z. L. Guo, K. Xu, and R. J. Wang, *Phys. Rev. E* **88**, 033305 (2013); Z. L. Guo, R. J. Wang, and K. Xu, *ibid.* **91**, 033313 (2015); Z. L. Guo and K. Xu, *Adv. Aerodyn.* **3**, 6 (2021).
- [6] Z. L. Guo and C. Shu, *Lattice Boltzmann Method and Its Applications in Engineering* (World Scientific Publishing, Singapore, 2013).
- [7] S. Marié, D. Ricot, and P. Sagaut, *J. Comput. Phys.* **228**, 1056 (2009).
- [8] E. Manoha and B. Caruelle, in *21st AIAA/CEAS Aeroacoustics Conference* (American Institute of Aeronautics and Astronautics, 2015), p. 2846.
- [9] L. M. Yang, C. Shu, J. Wu, and Y. Wang, *Comput. Fluids* **146**, 125 (2017).
- [10] G. Di Staso, S. Srivastava, E. Arlemark, H. Clercx, and F. Toschi, *Comput. Fluids* **172**, 492 (2018).
- [11] F. J. Alexander, S. Chen, and J. D. Sterling, *Phys. Rev. E* **47**, R2249 (1993).
- [12] Y. Qian, *J. Sci. Comput.* **8**, 231 (1993).
- [13] Y. Chen, H. Ohashi, and M. Akiyama, *Phys. Rev. E* **50**, 2776 (1994).
- [14] G. R. McNamara, A. L. Garcia, and B. J. Alder, *J. Stat. Phys.* **81**, 395 (1995).
- [15] N. Cao, S. Chen, S. Jin, and D. Martinez, *Phys. Rev. E* **55**, R21 (1997).
- [16] P. Lallemand and L.-S. Luo, *Int. J. Mod. Phys. B* **17**, 41 (2003).
- [17] X. W. Shan, *Phys. Rev. E* **55**, 2780 (1997).
- [18] X. Y. He, S. Y. Chen, and G. D. Doolen, *J. Comput. Phys.* **146**, 282 (1998).
- [19] Z. L. Guo, B. C. Shi, and C. G. Zheng, *Int. J. Numer. Methods Fluids* **39**, 325 (2002).
- [20] Z. L. Guo, C. G. Zheng, B. C. Shi, and T. S. Zhao, *Phys. Rev. E* **75**, 036704 (2007).
- [21] Q. Li, K. H. Luo, Y. L. He, Y. J. Gao, and W. Q. Tao, *Phys. Rev. E* **85**, 016710 (2012).
- [22] M. H. Saadat, F. Bösch, and I. V. Karlin, *Phys. Rev. E* **99**, 013306 (2019).
- [23] J. Latt, C. Coreixas, J. Beny, and A. Parmigiani, *Philos. Trans. R. Soc. A* **378**, 20190559 (2020).
- [24] J. Tölke, *J. Comput. Theor. Nanosci.* **3**, 579 (2006).
- [25] Y. L. Feng, P. Boivin, J. Jacob, and P. Sagaut, *J. Comput. Phys.* **394**, 82 (2019).
- [26] G. Farag, S. Zhao, T. Coratger, P. Boivin, G. Chiavassa, and P. Sagaut, *Phys. Fluids* **32**, 066106 (2020).
- [27] F. Renard, G. Wissocq, J.-F. Bousuge, and P. Sagaut, *J. Comput. Phys.* **446**, 110649 (2021).
- [28] X. W. Shan, X. F. Yuan, and H. D. Chen, *J. Fluid Mech.* **550**, 413 (2006).
- [29] N. Frapolli, S. S. Chikatamarla, and I. V. Karlin, *Phys. Rev. E* **93**, 063302 (2016).
- [30] P.-T. Lew, P. Gopalakrishnan, D. Casalino, R. Shock, Y. B. Li, R. Y. Zhang, and H. D. Chen, in *20th AIAA/CEAS Aeroacoustics Conference* (2014), p. 2755.
- [31] Y. L. Feng, P. Sagaut, and W.-Q. Tao, *J. Comput. Phys.* **303**, 514 (2015).
- [32] Z. L. Guo and T.-S. Zhao, *Phys. Rev. E* **67**, 066709 (2003).
- [33] T. Kataoka and M. Tsutahara, *Phys. Rev. E* **69**, 035701(R) (2004).
- [34] K. Qu, C. Shu, and Y. T. Chew, *Int. J. Mod. Phys. C* **18**, 447 (2007).
- [35] F. Chen, A. G. Xu, G. C. Zhang, Y. Li, and S. Succi, *Europhys. Lett.* **90**, 54003 (2010).
- [36] Y. Gan, A. Xu, G. Zhang, and H. Lai, *Proc. Inst. Mech. Eng. C* **232**, 477 (2018).
- [37] D. Wilde, A. Krämer, D. Reith, and H. Foyssi, *Phys. Rev. E* **101**, 053306 (2020).
- [38] D. Wilde, A. Krämer, D. Reith, and H. Foyssi, *Phys. Rev. E* **104**, 025301 (2021).
- [39] C. H. Sun, *Phys. Rev. E* **58**, 7283 (1998).
- [40] B. Dorschner, F. Bösch, and I. V. Karlin, *Phys. Rev. Lett.* **121**, 130602 (2018).
- [41] F. Nannelli and S. Succi, *J. Stat. Phys.* **68**, 401 (1992).
- [42] G. W. Peng, H. W. Xi, C. Duncan, and S.-H. Chou, *Phys. Rev. E* **58**, R4124 (1998).
- [43] S. Ubertini and S. Succi, *Prog. Comput. Fluid Dyn.* **5**, 85 (2005).
- [44] W. D. Li and L.-S. Luo, *Commun. Comput. Phys.* **20**, 301 (2016).
- [45] M. Sbragaglia and K. Sugiyama, *Phys. Rev. E* **82**, 046709 (2010).
- [46] W. D. Li and W. Li, *Comput. Fluids* **162**, 126 (2018).
- [47] T. Ohwada, *J. Comput. Phys.* **177**, 156 (2002).
- [48] Z. L. Guo, J. Q. Li, and K. Xu, *Phys. Rev. E* **107**, 025301 (2023).
- [49] L. H. Zhu, P. Wang, and Z. L. Guo, *J. Comput. Phys.* **333**, 227 (2017).
- [50] P. Wang, Y. Zhang, and Z. L. Guo, *Int. J. Heat Mass Transfer* **113**, 217 (2017).
- [51] T. Chen, X. Wen, L.-P. Wang, Z. L. Guo, J. Wang, and S. Y. Chen, *Phys. Fluids* **32**, 125104 (2020).
- [52] X. Wen, L.-P. Wang, and Z. L. Guo, *Phys. Fluids* **33**, 046101 (2021).
- [53] X. W. Shan, *J. Comput. Sci.* **17**, 475 (2016).
- [54] D. Wilde, A. Krämer, D. Reith, and H. Foyssi, *J. Comput. Sci.* **51**, 101355 (2021).
- [55] H. Liu, M. Kong, Q. Chen, L. Zheng, and Y. Cao, *Phys. Rev. E* **98**, 053310 (2018).
- [56] X. Nie, X. Shan, and H. Chen, *Phys. Rev. E* **77**, 035701(R) (2008).
- [57] K. H. Prendergast and K. Xu, *J. Comput. Phys.* **109**, 53 (1993).
- [58] Q. Li, Y. L. He, Y. Wang, and W. Q. Tao, *Phys. Rev. E* **76**, 056705 (2007).
- [59] C. K. Chu, *Phys. Fluids* **8**, 12 (1965).
- [60] V. A. Rykov, *Fluid Dyn.* **10**, 959 (1975).
- [61] P. Andries, P. Le Tallec, J.-P. Perlat, and B. Perthame, *Eur. J. Mech. B* **19**, 813 (2000).
- [62] L. C. Woods, *An Introduction to the Kinetic Theory of Gases and Magnetoplasmas* (Oxford University Press, Oxford, 1993).
- [63] B. Van Leer, *J. Comput. Phys.* **23**, 276 (1977).
- [64] R. Borges, M. Carmona, B. Costa, and W. S. Don, *J. Comput. Phys.* **227**, 3191 (2008).

- [65] P. Lallemand and L.-S. Luo, *Phys. Rev. E* **61**, 6546 (2000).
- [66] M. Geier, A. Greiner, and J. G. Korvink, *Phys. Rev. E* **73**, 066705 (2006).
- [67] J. Latt and B. Chopard, *Math. Comput. Simulat.* **72**, 165 (2006).
- [68] M. Geier, M. Schönherr, A. Pasquali, and M. Krafczyk, *Comput. Math. Appl.* **70**, 507 (2015).
- [69] P. D. Lax and X.-D. Liu, *SIAM J. Sci. Comput.* **19**, 319 (1998).
- [70] D. J. Lusher and N. D. Sandham, *AIAA J.* **59**, 533 (2021).
- [71] Z. J. Wang, K. Fidkowski, R. Abgrall *et al.*, *Int. J. Numer. Methods Fluids* **72**, 811 (2013).
- [72] Y. M. Qi, T. Chen, L.-P. Wang, Z. L. Guo, S. Y. Chen, *Phys. Fluids* **34**, 116101 (2022).